

# Noncontact three-dimensional mapping of intracellular hydromechanical properties by Brillouin microscopy

Giuliano Scarcelli<sup>1-3</sup>, William J Polacheck<sup>4</sup>, Hadi T Nia<sup>4</sup>, Kripa Patel<sup>1</sup>, Alan J Grodzinsky<sup>4-6</sup>, Roger D Kamm<sup>4,5</sup> & Seok Hyun Yun<sup>1,2,7</sup>

**Current measurements of the biomechanical properties of cells require physical contact with cells or lack subcellular resolution. Here we developed a label-free microscopy technique based on Brillouin light scattering that is capable of measuring an intracellular longitudinal modulus with optical resolution. The 3D Brillouin maps we obtained of cells in 2D and 3D microenvironments revealed mechanical changes due to cytoskeletal modulation and cell-volume regulation.**

The interaction between the liquid and solid phases in the cytoplasm regulates the rheological behavior of cells<sup>1</sup> and has a prominent role in determining how cells deform and move<sup>2</sup>. In turn, the hydromechanical properties of cells, such as the viscoelastic modulus and compressibility, influence intracellular water transport, cytoskeletal-network modulation and cell-volume regulation<sup>3</sup>. It is necessary to measure these properties *in situ* to study how cells regulate intracellular mechanics and how the properties change as cells interact with their microenvironment during aging and injury healing, as well as in the course of disease pathogenesis<sup>4</sup>. Mechanical techniques such as atomic force microscopy (AFM) and magnetic bead twisting have been widely used to measure the viscoelastic moduli and deformability of cells, and they have helped to elucidate the different mechanisms by which cells regulate mechanical properties such as cross-linking, branching and pre-stress in the cytoskeleton or variations in the solid-liquid volume fraction<sup>5</sup>. However, these techniques require contact with cells to impose mechanical stress, which limits their applicability to cells cultured on flat 2D substrates<sup>6</sup> or to micropatterned wells that maintain the 3D cell shape<sup>7,8</sup>. Optical tweezers or stretchers<sup>9</sup>, micropipette aspiration<sup>10</sup> and microfluidic deformation assays<sup>11</sup> have been used to

assess the elasticity of a cell in suspension, but without subcellular resolution. For cells that are confined in 3D hydrogels or microfluidic chips, particle-tracking microrheology<sup>12</sup> is potentially viable, but it requires the insertion of microbeads into cells and, if tracking subcellular components, it is influenced by motor activity<sup>13</sup>; furthermore, the resolution is limited by the number, size and random location distribution of the beads. Because of the limitations of these current methods, mapping of the mechanical properties of cells in a 3D meshwork of extracellular matrix proteins has not been performed yet<sup>14</sup>. As a result, there is a dearth of information on the biomechanical properties of cells in 3D environments and how they may differ from those of cells on a flat 2D substrate.

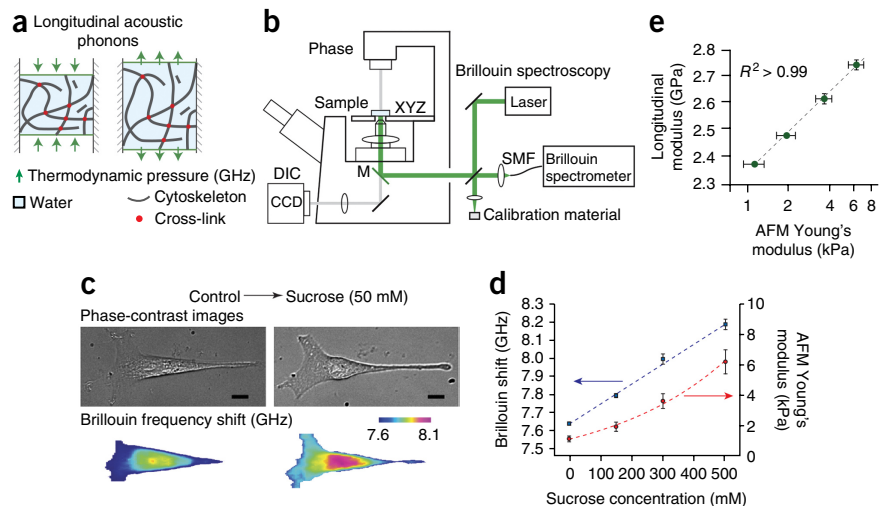
To address this need, we introduce Brillouin optical cell microscopy for noncontact, label-free and 3D mapping of intracellular and extracellular hydromechanical properties. This technique is based on the interaction of light with spontaneous acoustic phonons in the gigahertz frequency range<sup>15</sup>. By measuring the optical frequency shift of the scattered light, Brillouin measurements probe the local spontaneous pressure waves in intracellular environments, from which one can determine the high-frequency longitudinal modulus<sup>16</sup>. Mechanically, Brillouin interaction can be thought of as a test that measures the ratio of uniaxial stress to strain in confined compression conditions at high frequency<sup>17</sup> (**Supplementary Note 1** and **Supplementary Fig. 1**). The longitudinal modulus depends on intrinsic properties such as the modulus of individual cytoskeletal components, network cross-linking, the compressibility of the local microenvironment and the solid-liquid volume fraction (**Fig. 1a**). To enable cellular Brillouin mapping, we constructed a confocal Brillouin cell microscope by using a high-numerical aperture (0.6) objective lens that yields a spatial resolution of  $\sim 0.5 \times 0.5 \times 2 \mu\text{m}^3$  and a nonscanning parallel Brillouin spectrometer based on our previous design<sup>18</sup>, but with an enhanced spectral extinction of 70 dB, spectral resolution of 600 MHz and low loss ( $<10$  dB) (**Fig. 1b**, **Supplementary Note 2** and **Supplementary Fig. 2**), as well as a spectrum calibration arm (**Supplementary Note 3** and **Supplementary Fig. 3**). The light source was a 532-nm continuous-wave laser. With optical power levels of 2–4 mW at the sample and a spectral acquisition time of 0.1–0.2 s, the frequency-measurement sensitivity of the instrument was  $\sim 10$  MHz (**Supplementary Note 4** and **Supplementary Fig. 4**). This is about 0.1% of the Brillouin frequency shift of water (7.44 GHz at 18 °C).

To validate Brillouin microscopy for applications at the cellular scale, we investigated whether it is sensitive to liquid-solid regulation under different osmotic conditions. Adding sucrose to the cell medium generates osmotic pressure, which induces a substantial increase in cell elastic modulus<sup>19</sup>. Brillouin confocal sections of an

<sup>1</sup>Wellman Center for Photomedicine, Massachusetts General Hospital, Boston, Massachusetts, USA. <sup>2</sup>Department of Dermatology, Harvard Medical School, Boston, Massachusetts, USA. <sup>3</sup>Fischell Department of Bioengineering, University of Maryland, College Park, Maryland, USA. <sup>4</sup>Department of Mechanical Engineering, Massachusetts Institute of Technology, Cambridge, Massachusetts, USA. <sup>5</sup>Department of Biological Engineering, Massachusetts Institute of Technology, Cambridge, Massachusetts, USA. <sup>6</sup>Department of Electrical Engineering, Massachusetts Institute of Technology, Cambridge, Massachusetts, USA. <sup>7</sup>The Harvard-MIT Health Sciences and Technology Program, Cambridge, Massachusetts, USA. Correspondence should be addressed to G.S. ([scarc@umd.edu](mailto:scarc@umd.edu)) or S.H.Y. ([syun@hms.harvard.edu](mailto:syun@hms.harvard.edu)).

RECEIVED 27 MARCH; ACCEPTED 27 AUGUST; PUBLISHED ONLINE 5 OCTOBER 2015; DOI:10.1038/NMETH.3616

**Figure 1** | Principle and validation of Brillouin microscopy. **(a)** Schematic of the mechanical interaction probed by Brillouin scattering. Spontaneous fluctuations in density and pressure behave as microscopic mechanical perturbations from which the longitudinal modulus can be extracted with high-resolution optical spectroscopy. **(b)** Schematic of the instrument. A standard fluorescence microscope was modified to introduce the Brillouin excitation beam; the Brillouin scattered light is collected and coupled into a fiber, which serves as a confocal pinhole. The fiber delivers light into the Brillouin spectrometer (**Supplementary Note 2** and **Supplementary Fig. 2**). DIC, differential interference contrast; CCD, charge-coupled device; SMF, single-mode fiber. **(c)** Brillouin images (and coregistered phase-contrast images) of a cell before and after hyperosmotic shock. Scale bars, 10  $\mu\text{m}$ . **(d)** The effect of environmental osmolarity on both Brillouin and AFM-based micro-indentation measurements of cells. **(e)** Validation of Brillouin stiffness measurement against results of AFM-based micro-indentation tests for cells exposed to different levels of hyperosmotic shock. Each data point is the average of 8–11 measurements on different cells; error bars represent  $\pm$ s.e.m.



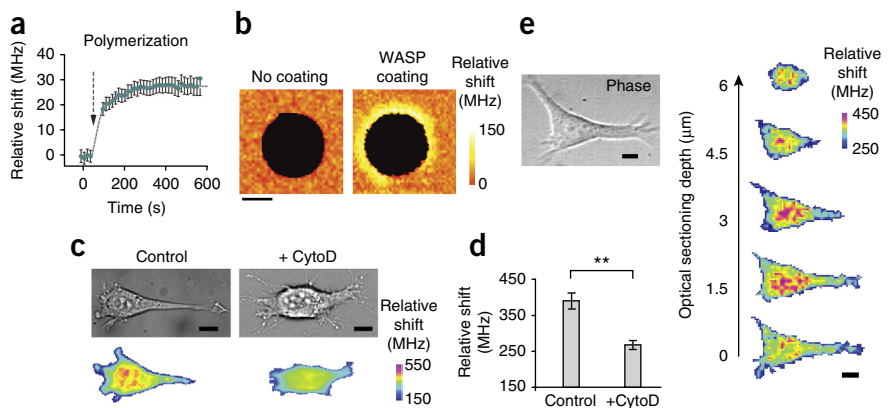
NIH 3T3 cell before and after hyperosmotic shock (50 mM of sucrose) showed a notable increase in Brillouin shift throughout the cell (**Fig. 1c**). To compute the mean longitudinal modulus, we averaged the Brillouin shifts over the cell volume and used estimated constant values for cell density and refractive index<sup>20</sup>. This was an approximation, as refractive index and density are not uniform throughout cells and likely change under different osmotic conditions; however, we estimated that the changes in refractive index and density did not substantially affect the modulus estimation (**Supplementary Note 5** and **Supplementary Fig. 5**). The measured Brillouin shift varied linearly with the concentration of sucrose (**Fig. 1d**).

For comparison with the current gold standard for measurements of the Young's modulus of cells, we performed micro-indentation by using an atomic force microscope equipped with a 5- $\mu\text{m}$ -diameter bead (**Supplementary Note 6** and **Supplementary Figs. 6–8**). The Young's modulus derived from the thin-layer Hertzian contact model of AFM indentation showed a nearly quadratic increase with sucrose concentration<sup>1,19</sup> (**Fig. 1d** and **Supplementary Fig. 6**). Typical values of the high-frequency longitudinal modulus are on the order of gigapascals, owing to the low compressibility of the intracellular microenvironment, and should not be interpreted as Young's or shear moduli of the cell, which are typically on the

order of kilopascals when measured at low frequencies<sup>6</sup>. However, our data showed a high correlation ( $R^2 > 0.99$ ) between the variations of these two types of moduli under the same environmental conditions (**Fig. 1e**). This result indicates that the underlying biochemical, physical and structural changes in the cell in response to the change in osmotic pressure affect both longitudinal and Young's moduli in the same direction. We have consistently observed such correlation in biological tissues<sup>21</sup>, as well as for synthetic hydrogels (**Supplementary Note 7** and **Supplementary Fig. 9**). Furthermore, in hydrogels, Brillouin signatures are sensitive to mechanical changes due to both polymer concentration and polymer cross-linking (**Supplementary Fig. 10**). The log-log linear relationship between the longitudinal modulus  $M'$  and Young's modulus  $E'$  is expressed as  $\log(M') = a \log(E') + b$ , where  $a$  and  $b$  are material-dependent coefficients<sup>21</sup>. Our instrument was able to detect a 0.05% change in the longitudinal modulus, which corresponds to 2% change in Young's modulus. This sensitivity is similar to, if not better than, that of contact-based mechanical measurements.

Cytoskeleton modifications are important in the regulation of cell mechanical properties. Using reconstituted actin gels *in vitro*, we verified that the Brillouin frequency shift was sensitive to two major mechanisms of cytoskeleton stiffening: actin

**Figure 2** | Brillouin microscopy measurements of mechanical changes *in vitro* and in a cell. **(a)** Brillouin frequency shift during actin polymerization into a gel. Data shown are relative to the Brillouin shift of 7.44 GHz for pure water at room temperature. **(b)** Brillouin microscopy images of the mechanical changes around beads promoting actin branching. Scale bar, 5  $\mu\text{m}$ . **(c)** Representative images of two different NIH 3T3 cells treated with cytochalasin D (+CytoD) or not treated (control). Scale bars, 10  $\mu\text{m}$ . **(d)** A reduction in Brillouin shift was observed between cytochalasin D-treated cells ( $N = 14$ ) and controls ( $N = 13$ ) when values were averaged over the whole cell volume (\*\* $P < 0.0001$ , unpaired two-tailed  $t$ -test). **(e)** Three-dimensional confocal reconstruction of the intracellular stiffness in an NIH 3T3 fibroblast cultured on a 15-kPa polyacrylamide gel substrate. Scale bars, 10  $\mu\text{m}$ . Error bars represent  $\pm$ s.e.m. in **a** and **d**.



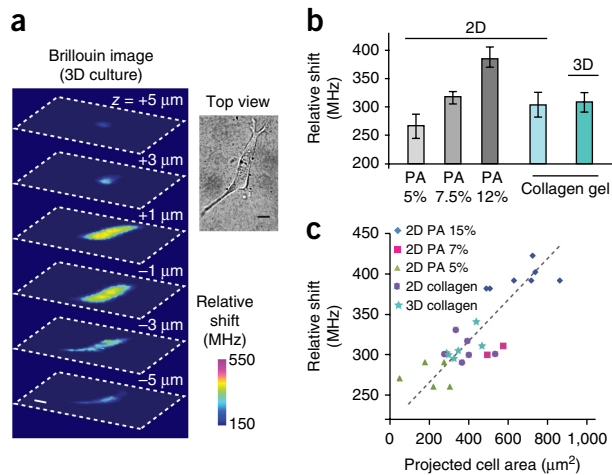


**Figure 3** | Effect of the extracellular matrix on cell stiffness.

(a) Representative 3D Brillouin image reconstruction of an NIH 3T3 cell cultured in a collagen gel matrix and the related top view obtained with bright-field microscopy ( $N = 5$ ). Scale bars, 10  $\mu\text{m}$ . (b) Average Brillouin shift of NIH 3T3 fibroblasts cultured on top of polyacrylamide (PA) gel substrates of (from left to right)  $\sim 1$  kPa ( $N = 8$ ), 2.5 kPa ( $N = 8$ ) and 15 kPa ( $N = 12$ ) and soft collagen gel substrates ( $\sim 300$  Pa) ( $N = 5$ ) compared with the average Brillouin shift of cells cultured in 3D collagen gels ( $N = 5$ ). Error bars represent  $\pm$ s.e.m. (c) Average Brillouin shift of NIH 3T3 fibroblasts plotted against the projected cell area in the different 2D and 3D microenvironments. Each symbol represents an individual data point.

polymerization (Fig. 2a) and branching of actin fibers with high spatial and temporal resolution (Fig. 2b). The Brillouin shifts increased as cells were spread on a 2D substrate (Supplementary Note 8 and Supplementary Fig. 11) and decreased when actin polymerization was inhibited with cytochalasin D (Fig. 2c,d). The confocal sectioning of Brillouin microscopy allowed us to analyze the longitudinal modulus with 3D resolution. The Brillouin images of an NIH 3T3 fibroblast cultured on a polyacrylamide gel substrate showed a stiffer nucleus and softer cytoplasm (Fig. 2e).

The noncontact nature of the Brillouin technique enables the mechanical measurement of cells in physiologic 3D collagen matrices (Fig. 3a). For direct comparison with cells in 2D, we measured cells grown on flat polyacrylamide substrates with shear moduli of 1, 2.5 and 15 kPa (Fig. 3b). Consistent with previous studies<sup>22</sup>, we observed an increase in Brillouin shift with increasing substrate rigidity. The Brillouin shift from cells cultured in 3D collagen gels with a shear modulus of  $\sim 300$  Pa was nearly identical to that of cells grown on top of the same collagen gels and was similar to those of cells grown on stiffer, 2.5-kPa polyacrylamide gels (Fig. 3b). Cells grown on polyacrylamide substrates with low moduli ( $\sim 1$  kPa) were partially rounded and not fully spread; in contrast, cells on 2D collagen gels and in 3D collagen gels ( $\sim 300$  Pa) appeared well spread. This morphological behavior has been attributed to the higher density of adhesion sites or the nonlinear elasticity of collagen gels<sup>23,24</sup>. We found a strong correlation ( $P < 0.001$ ) between cell stiffness and projected cell area (Fig. 3c). The data obtained on 2D substrates and in 3D hydrogels in various conditions collapsed on a single trend of cell stiffness versus maximum projected cell area (Fig. 3c). This finding, together with the identical intracellular moduli in 2D and 3D collagen gels, might indicate that cellular stiffness is similarly regulated in both 2D and 3D.

In conclusion, Brillouin optical microscopy enables mapping of the longitudinal moduli of live cells both on 2D substrates and in 3D matrices. The longitudinal modulus may not be directly linked to the tension in the cytoskeletal network or the cortical contractility<sup>25</sup>. However, Brillouin technology is sensitive to the biomechanical changes in a cell caused by factors such as biopolymer content, polymerization, branching and liquid-solid volume fraction. Brillouin microscopy opens up new research avenues for the biomechanical investigation of cells and their microenvironment in 3D at subcellular resolution.

## METHODS

Methods and any associated references are available in the online version of the paper.

Note: Any Supplementary Information and Source Data files are available in the online version of the paper.

## ACKNOWLEDGMENTS

We thank A.C. Martin, F.M. Mason, E. Moendarbary, M.C. Gather and K. Franze for helpful discussions, as well as H. Oda, K. Sawicki and K. Berghaus for help with hydrogel measurements. This work was supported in part by the National Institutes of Health (grants K25-EB015885 and R21-EY023043 to G.S.; grants R01-EY025454 and P41-EB015903 to S.H.Y.; and grant R33 CA174550 to R.D.K.), the National Science Foundation (grant CBET-0853773 to S.H.Y.) and a Human Frontier Science Program Young Investigator Grant (RGY0074/2013 to G.S.).

## AUTHOR CONTRIBUTIONS

G.S. and S.H.Y. conceived the project. G.S., W.J.P., R.D.K. and S.H.Y. devised the research plan. G.S. developed the instrument and performed the experiments. W.J.P. and K.P. developed cell protocols and performed cell-related control measurements. H.T.N., W.J.P. and A.J.G. designed and performed indentation experiments. G.S., W.J.P. and S.H.Y. wrote the manuscript with input from all other authors.

## COMPETING FINANCIAL INTERESTS

The authors declare no competing financial interests.

Reprints and permissions information is available online at <http://www.nature.com/reprints/index.html>.

1. Moendarbary, E. *et al. Nat. Mater.* **12**, 253–261 (2013).
2. Stroka, K.M. *et al. Cell* **157**, 611–623 (2014).
3. Stewart, M.P. *et al. Nature* **469**, 226–230 (2011).
4. Ingber, D. *Ann. Med.* **35**, 564–577 (2003).
5. Bao, G. & Suresh, S. *Nat. Mater.* **2**, 715–725 (2003).
6. Mofrad, M.R.K. & Kamm, R.D. *Cytoskeletal Mechanics* (Cambridge Univ. Press, 2006).
7. Ng, L. *et al. J. Biomech.* **40**, 1011–1023 (2007).
8. Lam, W.A., Rosenbluth, M. & Fletcher, D. *Blood* **109**, 3505–3508 (2007).
9. Guck, J. *et al. Biophys. J.* **81**, 767–784 (2001).
10. Evans, E. & Yeung, A. *Biophys. J.* **56**, 151–160 (1989).
11. Otto, O. *et al. Nat. Methods* **12**, 199–202 (2015).
12. Mason, T.G., Ganesan, K., vanZanten, J.H., Wirtz, D. & Kuo, S.C. *Phys. Rev. Lett.* **79**, 3282–3285 (1997).
13. Yap, B. & Kamm, R. *J. Appl. Phys.* **98**, 1930–1939 (2005).
14. Panorchan, P., Lee, J., Kole, T., Tseng, Y. & Wirtz, D. *Biophys. J.* **91**, 3499–3507 (2006).
15. Dil, J.G. *Rep. Prog. Phys.* **45**, 285–334 (1982).
16. Scarcelli, G. & Yun, S.H. *Nat. Photonics* **2**, 39–43 (2008).
17. Eisenberg, S.R. & Grodzinsky, A.J. *J. Orthop. Res.* **3**, 148–159 (1985).
18. Scarcelli, G. & Yun, S.H. *Opt. Express* **19**, 10913–10922 (2011).
19. Zhou, E.H. *et al. Proc. Natl. Acad. Sci. USA* **106**, 10632–10637 (2009).
20. Barer, R. & Joseph, S. Q. *J. Microsc. Sci.* **95**, 399–423 (1954).
21. Scarcelli, G., Kim, P. & Yun, S.H. *Biophys. J.* **101**, 1539–1545 (2011).
22. Solon, J., Levental, I., Sengupta, K., Georges, P.C. & Janmey, P.A. *Biophys. J.* **93**, 4453–4461 (2007).
23. Ali, M.Y., Chuang, C.-Y. & Saif, M.T.A. *Soft Matter* **10**, 8829–8837 (2014).
24. Winer, J.P., Oake, S. & Janmey, P.A. *PLoS One* **4**, e6382 (2009).
25. Nijenhuis, N., Zhao, X., Carisey, A., Ballestrem, C. & Derby, B. *Biophys. J.* **107**, 1502–1512 (2014).

## ONLINE METHODS

**Brillouin scattering.** Spontaneous Brillouin scattering arises from the interaction of light with acoustic phonons inside material. The Stokes frequency downshift occurs when light scattering generates an acoustic phonon. Anti-Stokes frequency upshift results when a photon gains energy from a phase-matched thermally generated acoustic phonon. In the approximation of an isotropic material in a probed voxel, the phase-matching acoustic frequency is given by  $\Omega = 2K(M'/\rho)^{0.5} \sin(\theta/2)$ , where  $K$  is the photon wavenumber,  $\theta$  is the angle between incident and scattered photons,  $M'$  is the real part of the material longitudinal modulus and  $\rho$  is the mass density of the sample. In backward (epi-) detection, the frequency shift at the peak of the Brillouin spectrum is given at  $\theta = \pi$  so that the real part of the longitudinal modulus is computed as  $M' = \rho\lambda^2\Omega^2/(4n^2)$ , where  $\lambda$  is the wavelength of the incident radiation and  $n$  is the index of refraction (**Supplementary Note 1**).

**Confocal microscope.** The light source of the Brillouin confocal microscope is a frequency-doubled Nd-YAG laser (Torus, Laser Quantum, Inc.) emitting a single longitudinal mode at 532 nm. The laser beam was cleaned with a single-mode spatial filter composed of a lens with a numerical aperture (NA) of 0.1 and a pinhole (Newport) with a hole size matched to the diffraction limit of the beam focus, recollimated and expanded with a lens of 125-mm focal length to overfill the back-aperture of the objective lens and inserted into an IX-71 microscope (Olympus). We cleared the optical path in the right-side port of the microscope and inserted a 100% reflection mirror just below the filter-cube turret. This mirror reflected the laser beam to the sample through an empty slot of the turret and directed the Brillouin light back-scattered from the sample out of the microscope through the same port. Light was focused onto the cell sample by an objective lens of NA 0.6 in epi-illumination, with spatial resolution of  $\sim 0.5 \times 0.5 \times 2 \mu\text{m}^3$ . For calibration, we used a pair of automated shutters and reference materials (**Supplementary Fig. 3**). For 3D imaging, a Brillouin spectrum was acquired from each location in the sample, and then the sample was translated stepwise using three-axis motorized stages (Prior). Scattered light from the samples was collected by a single-mode optical fiber (460HP, Thorlabs), which also served as a confocal pinhole, and delivered to the apodized VIPA spectrometer (**Supplementary Fig. 2**). With 2–4 mW illumination power at the sample, it generally took 2–5 min to acquire a 2D frame, depending on the number of pixels. In these conditions, cell morphology was not affected during repeated measurements, and no apparent difference in mechanical properties was observed between fresh cells and cells that were imaged multiple times. At higher powers exceeding 10 mW, cells remained viable, but they tended to change their shape after the imaging session.

**VIPA spectrometer.** The spectrometer consisted of two apodized cross-axis VIPA stages with a relay telescope and square-hole spatial filter between them (**Supplementary Note 2**). The two VIPA etalons had identical specifications ( $R_1 = 99.9\%$ ,  $R_2 = 95\%$ ,  $1.6^\circ$  internal tilt, Light Machinery). Linearly variable intensity filters (Rugate and Newport 50FS04DV) were used for apodization. The diffraction pattern after the final VIPA stage was detected with an electron-multiplying charge-coupled device (EM-CCD) camera (Ixon Du197, Andor) with a dispersion slope of 0.3 GHz/pixel.

**Data acquisition and analysis.** We used LabView for instrument automation, using modified manufacturer sample codes (Prior translational stages, Andor camera) and home-written codes to operate shutters. We used Matlab for spectral analysis. Our algorithm (provided as **Supplementary Software**) extracts the optical spectrum and measures the Brillouin shift and magnitude by curve-fitting with Lorentzian profiles (**Supplementary Fig. 3**). Brillouin images were produced in Matlab, typically using the “jet” colormap with red replaced by magenta. To quantify the average Brillouin shift of a cell, we typically acquired several *en face* sections of the cell under examination at different heights (similarly to **Fig. 2e**). After the measurement, we identified the voxels to average (i.e., belonging to the cell rather than the surrounding medium) using a threshold on Brillouin shift and linewidth.

**Cell culture on 2D substrates.** An NIH 3T3 fibroblast cell line tested for mycoplasma contamination was purchased from American Type Culture Collection (ATCC); after purchase, cells were frozen at early passage, and a fresh cell culture was routinely started from frozen stock. We maintained the cells and inspected them daily under an inverted-phase microscope to compare their morphology at different cell densities against reference images. Cells were grown on custom-made 2D substrates consisting of a collagen-coated polyacrylamide gel layer attached to 20-mm glass-bottom dishes. Glass-bottom dishes were first treated with 200  $\mu\text{l}$  of (3-aminopropyl)trimethoxysilane for 3 min and 400  $\mu\text{l}$  of 0.5% glutaraldehyde solution for 30 min to condition the glass for attachment to polyacrylamide. We then deposited 15–30  $\mu\text{l}$  of polyacrylamide solution with 5–12% acrylamide and 0.04–0.4% bis-acrylamide in each glass well to create 50–100- $\mu\text{m}$ -tall gels. Circular coverslips treated with Rain-X (ITW Global Brands) were placed face-down on the gel to create a flat, even surface. After the gels had solidified, the coverslips were discarded and the gels were treated with 1 ml of hydrazine hydrate for 4 h, followed by 2 ml of 5% glacial acetic acid for 1 h to allow attachment of collagen (type I from rat-tail) to the polyacrylamide gel. Gels were then washed with PBS three times for 30 min each time, sterilized under UV light and left overnight under a layer of 1.5 mg/ml oxidized collagen<sup>26</sup>. Gels were then washed in serum-free Dulbecco's modified Eagle's medium (DMEM) three times for 30 min each time and left in DMEM for at least 24 h before cell plating. Cells were plated on the gel substrate in DMEM supplemented with 10% FBS and allowed to spread for at least 24 h before imaging.

**Osmotic pressure experiments.** Hyperosmotic environments of varying strength were imposed on cells by the addition of 2 $\times$  strength sucrose solutions of 0, 150, 300 or 500 mOsm in equal volume to the existing cell media. We made sucrose solutions by dissolving sucrose in DMEM supplemented with 1% FBS and sterilizing it for 30 min under UV light. Cells were grown on polyacrylamide gels, and the cell media was switched to DMEM supplemented with 1% FBS at least 6 h before sucrose was added or overnight. Cell stiffness was measured before and immediately after sucrose addition with Brillouin microscopy and with AFM for comparison. To supplement AFM measurements, we obtained average cell dimensions using confocal microscopy (**Supplementary Note 6**).

**AFM-based micro-indentation.** An Asylum MFP3D atomic force microscope (Asylum Research, Santa Barbara, CA) was used to perform the nanoindentation on single fibroblasts that were adhered to the polydimethylsiloxane-coated substrate. The cells were indented by gold-coated polystyrene colloidal probe tips (end radius  $R \sim 2.5 \mu\text{m}$ ) attached to cantilevers with a nominal spring constant  $k \sim 0.06 \text{ N/m}$  (Novascan, Ames, IA). We applied the thermal noise oscillation method to determine the cantilever spring constant for each probe tip<sup>27</sup>. The indentation was performed under a force control scheme, with a maximum force of  $\sim 2.5 \text{ nN}$ . The resulting indentation depths were in the range of  $0.2\text{--}1 \mu\text{m}$ . The axial ( $z$ -direction) displacement of the tip was calculated as the  $z$ -piezo subtracted from the vertical deflection of the cantilever. Typical force-displacement curves for cells in different sucrose concentrations are shown in **Supplementary Figure 7**. A typical force-displacement curve and the best-fit curve from the thin-layer Hertz model are shown in **Supplementary Figure 8**. We indented different locations on cells to obtain an average for the Young's modulus of each cell. An indentation speed of  $0.1 \mu\text{m/s}$  was used to probe the Young's modulus under close-to-equilibrium conditions.

**Reconstituted actin gel polymerization and branching.** Branching F-actin was polymerized on polystyrene spheres pre-coated with *Viscum album* L. var. *coloratum* agglutinin (VCA), according to the protocol outlined by Pujol *et al.*<sup>28</sup>. An actin polymerization kit, VCA-Domain WASP protein, ARP2/3 protein, cofilin and gelsolin were all obtained from Cytoskeleton and handled according to the provided instructions.  $4.5\text{-}\mu\text{m}$  carboxylated polystyrene spheres (Spherotech) were coated in VCA and added to actin buffer solution to polymerize the actin at  $6.5 \mu\text{M}$  actin,  $6.5 \mu\text{M}$  cofilin,  $90 \text{ nM}$  gelsolin,  $180 \text{ nM}$  ARP2/3 and  $0.01\%$  VCA. To stop polymerization, we diluted the actin solution 1:10 with  $6.6\text{-}\mu\text{M}$  phalloidin. Beads were allowed to settle on a gel substrate to reduce motion and were imaged immediately thereafter. We also imaged the beads with confocal microscopy, for which we modified the dilution step to include  $10\%$  Alexa Fluor 594 phalloidin (Life Technologies).

**Actin disruption via cytochalasin D.** We achieved actin-filament disruption in NIH 3T3 cells by submerging cells in

$5 \mu\text{g/ml}$  cytochalasin D (Sigma-Aldrich) in DMEM supplemented with  $1\%$  FBS. Cells were plated in DMEM supplemented with  $10\%$  FBS at least  $24 \text{ h}$  before imaging, and cell media was switched to DMEM supplemented with  $1\%$  FBS at least  $6 \text{ h}$  before to serum starve the cells and reduce cell movement during imaging. Cells were imaged  $30 \text{ min}$  to  $1 \text{ h}$  after the addition of a stock solution of cytochalasin made in DMEM.

**Cell culture in 3D collagen gels.** Rat tail collagen type I in acetic acid (BD Biosciences) was buffered with  $10\times$  PBS with phenol red, titrated to a pH of  $8.0$  with  $0.1 \text{ M}$  sodium hydroxide, and brought to a final concentration of  $2 \text{ mg/mL}$  with water. Cells were lifted from culture with Trypsin-EDTA, centrifuged at  $200g$  for  $5 \text{ min}$ , resuspended in growth medium and mixed with collagen I solution for a final concentration of  $4 \times 10^5$  cells per milliliter of total collagen solution. Collagen was polymerized in humidified chambers at  $37 \text{ }^\circ\text{C}$  and  $5\% \text{ CO}_2$  for  $20 \text{ min}$  before growth medium was added to hydrate the gel.

**Dependence of cell stiffness on spread area.** To quantitatively assess the cell stiffness-morphology relationship, we measured the average cell stiffness versus the projected cell area for several conditions. For each cell, we estimated the Brillouin shift by averaging the frequency shift at each pixel in the cell; we estimated the projected cell area by determining the cell contour from the phase-contrast image and computing the enclosed area with ImageJ. In the 3D cultures, only cells with extended morphology were analyzed, and round cells were discarded. In plots, each data point corresponds to a different cell. The points were fit to the same linear regression curve ( $R > 0.8$ ,  $P < 0.001$ ).

**Code availability.** The Matlab code used to analyze data is provided as **Supplementary Software** along with representative **Supplementary Data** to run the code.

26. Damjanović, V., Lagerholm, B. & Jacobson, K. *Biotechniques* **39**, 847–851 (2005).
27. Hutter, J.L. & Bechhoefer, J. *Rev. Sci. Instrum.* **64**, 1868 (1993).
28. Pujol, T., du Roure, O., Fermigier, M. & Heuvingh, J. *Proc. Natl. Acad. Sci. USA* **109**, 10364–10369 (2012).